Combustion and Flame 156 (2009) 1514–1524

Contents lists available at ScienceDirect

Combustion and Flame

journal homepage: www.elsevier.com/locate/combustflame

Soot properties of laminar jet diffusion flames in microgravity

F.J. Diez [a], C. Aalburg [b], P.B. Sunderland [c], D.L. Urban [d,*], Z.-G. Yuan [d], G.M. Faeth [b]

[a] Rutgers University, Piscataway, NJ 08854, USA
[b] University of Michigan, Ann Arbor, MI 48109, USA
[c] University of Maryland, College Park, MD 20742, USA
[d] NASA Glenn Research Center, 21000 Brookpark Rd., Cleveland, OH 44135, USA

ARTICLE INFO

Article history:
Received 28 March 2008
Received in revised form 1 April 2009
Accepted 11 April 2009
Available online 28 May 2009

Keywords:
Laminar flamelets
Non-buoyant flames
Non-premixed flames
Soot

ABSTRACT

The soot properties of round, non-buoyant, laminar jet diffusion flames are described, based on experiments carried out in microgravity conditions during three flights of the Space Shuttle Columbia (Flights STS-83, 94 and 107). Experimental conditions included ethylene- and propane-fueled flames burning in still air at an ambient temperature of 298 K and ambient pressures of 35–100 kPa. Measurements included soot volume fraction distributions using deconvolved laser extinction imaging and soot temperature distributions using deconvolved multiline emission imaging. Mixture fractions were estimated from the temperature measurements. Flow field modeling based on the work of Spalding is presented. It is shown that most of the volume of these flames is inside the dividing streamline and thus should follow residence time state relationships. Most streamlines from the fuel supply to the surroundings exhibit nearly the same maximum soot volume fraction and maximum temperature. The present work studies whether soot properties of these flames are universal functions of mixture fraction, i.e., whether they satisfy soot state relationships. Soot state relationships were observed, i.e., soot volume fraction was found to correlate reasonably well with estimated mixture fraction for each fuel/pressure selection. These results support the existence of soot property state relationships in steady non-buoyant laminar diffusion flames, and thus in a large class of practical turbulent diffusion flames through the application of the laminar flamelet concept.

Published by Elsevier Inc. on behalf of The Combustion Institute.

1. Introduction

Soot reaction properties in flames represent an important unsolved combustion problem having significant relevance to society. For example, particulate soot emitted as a pollutant from combustion processes causes more deaths than any other combustion-generated pollutant, e.g., it is responsible for roughly 50,000 premature deaths each year in the US alone [1]. In addition, carbon monoxide emissions that result as a direct by-product of particulate soot emissions are a leading cause of death in unwanted fires, e.g., they are responsible for most of the roughly 4000 fire deaths each year in the US alone. Furthermore, continuum radiation from particulate soot is mainly responsible for the growth and spread of unwanted fires. Finally, limited understanding of the complex processes that cause particulate soot to form in the high-temperature regions of flames is a major impediment to the development of robust methods of computational combustion needed for the advancement of practical combustor designs. Taken together, these observations amply motivate the study of soot processes in flames.

Soot processes in turbulent non-premixed (diffusion) flames are of greatest practical interest; however, detailed transient measurements of soot processes in turbulent flames are not feasible using existing technology [2]. Prior work has shown that results for laminar flames can be directly relevant to turbulent diffusion flames through the laminar flamelet concept [3], where turbulent flames are treated as collections of laminar flamelets [4,5]. The laminar flamelet approach has been applied in numerous laminar and turbulent flame models [6,7]. Unfortunately, buoyant laminar diffusion flames have not been found to have corresponding utility for studying soot processes. Thus, a major objective of the present investigation is to determine whether the laminar flamelet concept can be applied to soot properties in non-buoyant laminar diffusion flames. Past research concerning soot properties in laminar diffusion flames is only discussed briefly here; for more extensive reviews see [8–11], and references cited therein.

The structure of steady, non-buoyant, laminar diffusion flames is a fundamental combustion problem that has attracted significant attention in the literature since the classical study of Burke and Schumann [12]. This interest continues because this simple flame configuration enables a better understanding of the combined effects of convection, heat and mass transport and chemistry, which control flame structure and flame response to varying

* Corresponding author.
E-mail address: david.l.urban@nasa.gov (D.L. Urban).

0010-2180/$ - see front matter Published by Elsevier Inc. on behalf of The Combustion Institute.
doi:10.1016/j.combustflame.2009.04.006

Nomenclature

d	burner inside diameter
f	mixture fraction
f_s	soot volume fraction
g	earth gravity; gray level before filtering
G	gray level after filtering
I_u	jet momentum
L_f	luminous flame length
m	fuel mass flow rate
p	pressure
q_0	burner volumetric flowrate
r	radial coordinate
Re	Reynolds number ($=u_0 d/\nu$)
t	residence time
T	temperature
u	axial velocity
z	height above burner

Greeks

η	dimensionless volumetric flow rate
ν	fuel kinematic viscosity at 298 K
ξ	dimensionless radial coordinate

Subscripts

0	burner tube condition
ch	characteristic value
i	index
st	stoichiometric condition

flow conditions characteristic of practical turbulent flames. The earliest studies of this type employed ground-based (drop tower and aircraft) microgravity facilities [13,14]. Some recent developments in the study of diffusion flames in microgravity (parabolic flights) include the study of the sooting behavior and the soot volume fraction of planar boundary layer laminar diffusion flames, see Legros et al. [15], and Fuentes et al. [16], and the study of the sooting behavior of burning droplets [17] and spherical flames [18] in microgravity.

The development of computationally tractable ways to simulate the structure of soot-containing flames provides motivation for the present investigation. The methodology considered here is described by Bilger [19] and Lockwood and Naguib [20] through implementation of the conserved-scalar formalism in turbulent diffusion flames. This methodology is advanced by the observation of Bilger [19] that gas-phase scalar properties in laminar diffusion flames could be correlated solely as functions of mixture fraction, even in the fuel-rich regions of flames that are affected by finite rate fuel decomposition and soot chemistry. Bilger also proposed that these correlations from laminar flames, called state relationships, could be applied to turbulent flames, assuming that turbulent flames correspond to wrinkled laminar flames. This approach allows estimation of all scalar gas-phase properties in a turbulent flame given knowledge of the distribution of a single conserved-scalar property such as the mixture fraction. There are however some limitations to the flamelet concept. Bilger et al. [21] and Bilger [22] suggest that there is a range of validity for the flamelet models, not yet clearly specified, for which the model should not be applied. This involves flames with large variation in scalar dissipation and when the advection term in the transport equation is important. Fortunately, there are emerging models that extend and modify the flamelet model for these particular cases [23–27].

Two global flame properties of turbulent diffusion flames, described below, have been reported that provide evidence that these flames might satisfy universal state relationships for soot properties. Soot-containing, buoyant, turbulent flames exhibit constant yields of combustion products per unit mass of fuel burned for a given fuel, independent of fire size [28,29]. In addition, the soot emitted from these flames exhibits the same morphology regardless of where the soot is emitted from the flame [29,30]. These properties suggest that soot state relationships might exist in these flames.

The laminar flamelet concept simplifies analyses of the scalar structure of turbulent diffusion flames. It has been effective for predicting the structure and radiation properties of buoyant turbulent diffusion flames that have negligible continuum radiation from soot [4,31–39]. When chemistry is sufficiently fast, scalar properties are only functions of the degree of mixing between the fuel and oxidizer owing to the approximate equality of mass and heat diffusivities in flames. State relationships can be measured in steady laminar jet diffusion flames, allowing properties to be predicted in unsteady reacting systems (for which detailed computations generally are impossible). Successful correlations of flame scalars including soot have been obtained from temporally averaged measurements in turbulent flames [48], and these are useful for predicting temporally averaged behavior but not for predicting instantaneous properties.

A state relationship combustion model was combined with two different soot models by Zimberg et al. [40] to study coupled turbulence, soot chemistry, and radiation interactions. One soot model was a soot state relationship and the other used finite rate soot kinetics. The soot state relationship model reduced computation time significantly and was successful at reproducing many of the features of the flame structure, although it did not fully capture some details seen with finite rate chemistry. Pitsch et al. [41] had good success predicting soot properties of a turbulent gas jet using a hybrid model, which combined a simplified soot model with a flamelet model to predict the gas-phase species. Aksit and Moss [42] reported success modeling a turbulent jet with a hybrid model for sooting hydrocarbon combustion that combined a two-step soot model with the flamelet approximation for the remaining scalars. A simplified model for soot formation and oxidation in a computational fluid dynamics (CFD) simulation of non-premixed hydrocarbon flames was developed by Lautenberger et al. [10]. Lignell et al. [2] and Yoo and Im [43] predicted flame properties, including soot concentrations, using direct numerical simulation (DNS) in a 2D configuration using simplified kinetics for both the overall fuel chemistry and for the soot processes. These works show considerable promise in predicting soot concentrations in flames through simplified kinetics or flamelet models, nevertheless there remain opportunities for the use of state relationships.

Given the promising results seen for the laminar flamelet concept when applied to predicting species concentrations in soot-containing laminar diffusion flames, attempts were made to apply this concept to the structure and radiation properties of soot-containing buoyant turbulent diffusion flames involving acetylene and ethylene burning in air at atmospheric pressure [5,45–47]. Owing to measurement limitations, these experiments either studied laminar flames or used temporally averaged soot volume fraction and temperature or mixture fraction measurements in turbulent flames. Success was seen in the temporally averaged turbulent correlations at locations away from the burner and in effectively predicting average parameters such as soot concentration or radiation. However, the laminar results also showed significant effects of the

intrusion of buoyancy, which produced differences in the correlation of soot concentration with mixture fraction at different axial locations [44]. More recently, D'Anna et al. [48] revisited the work of Kent and Honnery [47] and examined the correlation of soot volume fraction with mixture fraction in turbulent ethylene flames using soot concentrations from time-averaged laser-induced-incandescence measurements and mixture fractions from time-averaged predictions. As in the prior work [47] residence time effects were seen but the use of time-averaged measurements in turbulent flames remains a concern.

In turbulent flames, local effects of buoyancy are small in comparison with viscous effects. This is because in the Kolmogorov scale, the Reynolds number is always one, whereas the Grashof number is to the third power of the Kolmogorov scale. Thus the Grashof number diminishes quickly when the Kolmogorov scale gets smaller, i.e., the flame gets more turbulent. For instance, for a turbulent flame with an integral length scale of 0.25 m, typical for a flame issued from a single jet, locally the Grashof number is only one tenth of the Reynolds number when the integral Reynolds number is greater than 2300. On the other hand, because soot particles do not diffuse significantly, they are mainly convected by flow in laminar diffusion flames, causing different behavior in laminar non-buoyant and buoyant flames. This is the main cause for the failure to find soot property state relationships in buoyant laminar flames [5,46,49]. In buoyant flames the dividing streamline, which originates from the edge of the burner, remains close to the axis. As a result, soot particles that form near the flame sheet will pass through the fuel-rich region of the flame and then pass back through the flame sheet near its tip. In contrast, in non-buoyant flames the dividing streamline diverges from the axis and bounds a large fraction of the flame volume such that most soot particles form near the cool core of the flame and are drawn directly toward and through the flame sheet. Despite the convenience of studying steady laminar flames, given these differences, establishment of universal state relationships for buoyant laminar flames is improbable, and the hypotheses of this work are that soot state relationships exist for non-buoyant, laminar, jet diffusion flames [50–52] and that these can be applied in turbulent flame computations, providing better correlations than temporally averaged correlations. Ground-based efforts to study reduced-buoyancy flames were unable to provide the gravitational environment and residence time needed for these studies [49,53–55]. Although it is expected that state relationship models will not cover the intricacies of all of the turbulent flamelet structure (e.g., at regions of high curvature), if these models predict the soot properties in a large portion of the flame envelope, the approach will be a useful predictor of soot properties in practical turbulent flames.

1.1. Objectives

Experiments were carried out with non-buoyant round laminar jet diffusion flames at long-term microgravity conditions on board the Space Shuttle Columbia (Flights STS-83 and 94). Unfortunately, most of the flames considered during these experiments had large characteristic residence times that resulted in significant radiant heat losses and rendered them not useful for state-relationship studies. For these flames, radiative heat losses tend to have the largest influence near the flame tip, where convective velocities and rates of reaction become small, resulting in a tip-opening phenomenon that is not typical of laminar flamelets encountered in practical turbulent diffusion flames [49]. Radiative heat losses and tip-opening phenomena are not typical of conditions considered during development of the simplified flame structure analysis of Spalding [56], whereas tip opening with unburned fuel passing out of the flame along its axis clearly involves loss of universal state relationships.

In view of these results, additional observations of soot-containing, steady, non-buoyant laminar jet diffusion flames were undertaken in microgravity on Space Shuttle Columbia during Flight STS-107, with the following specific objectives:

1. Derive an expression for the location of the dividing streamline, the streamline that originates from the edge of the burner, from the modified Spalding streamlines [56] for non-buoyant flames.
2. Derive a state relationship for residence time along the centerline of non-buoyant gas jet flames.
3. Measure soot temperatures, soot volume fractions, and flame shapes for various fuels, fuel flow rates, burner diameters and pressures in still air environments, considering quasi-steady non-buoyant laminar jet diffusion flames with small radiative heat losses.
4. Exploit the measurements to determine whether soot property state relationships exist within non-buoyant and nearly adiabatic, steady, laminar diffusion flames, which would demonstrate that these flames are the proper paradigm for soot processes in practical turbulent diffusion flames.

2. Experimental methods

2.1. Test conditions

Test conditions for seven of the flames observed on Space Shuttle Columbia Flights STS-83, STS-94 and STS-107 are summarized in Table 1. Details of the experimental design are in Urban et al. [49] and the operating conditions are discussed in detail in Aalburg et al. [57]. Complete descriptions of the information obtained from these experiments, along with a summary of the background and motivation for carrying out long term experiments at microgravity using the orbiting Space Shuttle Columbia, can be found in [49,57–61]. The flame lengths and the sooting conditions were determined from the luminous images in the video recordings; all of the other table entries were preset operating conditions. The Reynolds number was computed based upon the conditions at the burner exit. The flames were stabilized at the exit of a round nozzle located along the axis of a windowed, cylindrical chamber. The chamber had a diameter of 400 mm; a maximum length of 740 mm; an internal volume of 0.082 m^3; and was operated at pressures of 35–130 kPa. Prior to each test, the chamber was vented to space and then filled with oxygen/nitrogen mixtures to provide the nominal composition of dry air (21 ± 1% oxygen by volume). Owing to the sealed chamber, the pressure, temperature and composition of the gas surrounding the test flames all varied gradually during the flame lifetime. The greatest change involved the composition of the gas within the chamber; however, test conditions were controlled so that the maximum oxygen consumption generally did not reduce the oxygen mole fraction by more than 0.02 during each experiment. Over the test series reported here, the two different fuel nozzles that were used were constant-diameter, cylindrical, stainless-steel tubes, having inside diameters of 0.80 and 1.60 mm and lengths of 148 mm from the inlet plenum. The inlets of the nozzles had flow straighteners to prevent swirl, and the overall length-to-diameter ratios of the passages were greater than 55:1, which was sufficient to yield fully developed laminar pipe flow at the nozzle exit. The test fuels were stored in cylinders and were delivered to the nozzles through a solenoid valve, a mass-flow-rate controller and a flow-limiting orifice. The flames were ignited by a hot wire coil that was retracted from the nozzle exit after ignition. The first set of experiments were conducted on

Table 1
Summary of the test flames.[a]

Test[b]	Fuel	Sooting condition[c]	d (mm)	p (kPa)	m (mg/s)	u_0 (m/s)	Re	L_f (mm)	Time[d] (s)
41E107	C_2H_4	SC	0.8	100	0.65	1.12	98	17.1	254
17E94	C_2H_4	SP	1.6	35	1.34	1.69	100	34.0	66
02E94	C_2H_4	SC	1.6	50	0.76	0.67	57	17.7	32
03E94	C_2H_4	SP	1.6	50	1.29	1.14	97	36.5	91
03E83[e]	C_2H_4	SE	1.6	50	1.84	1.63	138	63.0	91
46P107	C_3H_8	SC	0.8	99	0.53	0.59	100	15.8	254
08P107	C_4H_8	SE	0.8	100	1.21	1.33	229	32.1	223

[a] Many entries here are reproduced from Aalburg et al. [57].
[b] E is ethylene, P is propane, and numbers 83, 94, and 107 denote missions STS-83, STS-94, and STS-107.
[c] All flames had closed tips. SC is soot containing, SE is soot emitting, and SP is smoke point.
[d] Time is defined as the elapsed time between ignition and image acquisition for soot volume fraction and temperature.
[e] Note that this flame's identifier was 02E in Urban et al. [49].

STS-83 and 94 in 1997 using the larger nozzle. As described by Urban et al. [49], these flames exhibited substantial radiative cooling due to the long residence time characteristic of these nozzles. This cooling led to tip-opening and sooting behavior not consistent with the laminar flamelet concept. The experiments conducted on STS-107 employed the smaller nozzle sizes to produce lower residence time flames that could be expected to produce state-relationship behavior. However, during the mission, communication difficulties with the orbiter prevented the down-linking of the data from approximately half the tests and the tragic loss of the orbiter and crew destroyed the stored records for the soot diagnostics.

Although the three flight missions included more flames than are presented in Table 1 [57], the tests that were suitable for state-relationship analysis were limited to those presented in Table 1. The other flames were not used for reasons including: excessive residence time and consequent radiative cooling; soot concentrations below the sensitivity threshold of the laser extinction system; and loss of the soot data due to the loss of the spacecraft.

2.2. Instrumentation

Flame operation was monitored by making the following measurements: fuel flow rate with an accuracy of 0.8% of reading; fuel temperatures at the nozzle inlet with an accuracy of ±1.5 °C; chamber pressures with an accuracy of 1.2% of reading; and chamber gas temperatures (far from the flames) with an accuracy of ±1 °C. These measurements were recorded at a frequency of 1 Hz. Soot-luminosity boundaries and flame-sheet locations were measured from images obtained using color charge-coupled device (CCD) video cameras (Hitachi Model KP-0553 during flights STS-83 and STS-94, and Panasonic Model WV-CD612 during flight STS-107). The cameras had a 125 × 164 mm field of view and a depth of field of 25 mm centered on the flame axis. The spatial resolution of recorded images was better than 0.3 mm. Color flame images were recorded at 30 images/s. Measured luminous flame lengths and diameters have estimated experimental uncertainties (95% confidence) that are less than 10%; the major component in the error is attributed to the effect of the camera gain setting.

The imaging methods developed by Greenberg and Ku [62] were used to produce laser extinction images for chord-like paths through the flames. These images were deconvolved to obtain soot volume fraction distributions. The laser source was a laser-diode yielding 1 mW of optical power at 634 nm coupled through an optical fiber. The expanding laser beam from the fiber tip then passed through a custom apodizing filter (to reduce intensity variations) and then was collimated by an off-axis parabola and directed by a rectangular turning mirror, producing a 38 × 80 mm beam that passed through the flame and the region above the flame. In the flame region, the variation of background laser intensity is less than 40% for STS-83 and 94 and 60% for STS-107. The signal transmitted though the flame was collected by a decollimator equipped with a laser line filter (1–2 nm full-width-half-max, FWHM) and a 3.8 mm diameter spatial filter before being received by a CCD video camera (Panasonic GP-MF552). The output of the camera was converted to digital images by a video digitizer. The camera was oriented to provide 377 pixels over the 80 mm field of view along the flame axis and 227 pixels over 38 mm in the radial direction. The laser was adjusted to bring the intensity maximum in the field of view just below saturation of the CCD camera to allow optimum use of the 8-bit digitizer sensitivity. Spatial resolution of the imaging system was better than 0.3 mm. Background measurements of the laser beam intensity distribution were made with no flame present before and after each run. The extinction measurements were analyzed assuming Rayleigh scattering from primary soot particles with refractive indices from Dalzell and Sarofim [63].

Soot temperature distributions were obtained by two-color pyrometry via deconvolution of radiation intensities for chord-like paths through the flames. The procedure involved considering the 650/850 nm line pair. The flame images were observed using two CCD cameras (Panasonic GP-MF552) with appropriate interference (10 nm FWHM band pass) filters in addition to neutral density filters (to control overall signal levels) in the optical path. Two digitizers were used to convert the outputs of the two cameras to digital images. Two cameras were mounted side-by-side and were oriented to provide 225 pixels over the 80 mm field of view along the flame axis and 77 pixels over the 20 mm wide region that includes the soot-containing region. The integration time of the cameras was controlled to enable optimal use of the CCD detectors. The spatial resolution was better than 0.4 mm. Camera response at the two wavelengths was calibrated with a blackbody source. The measurements were analyzed assuming Rayleigh scattering from the soot particles similar to the extinction measurements.

The flame images obtained, either from laser extinction for soot volume fraction measurements or from flame emission for soot temperature measurements, are projections onto the 2D imaging plane. Since these flames are axisymmetric, the deconvolution is carried out by Abel transform. To reduce the effects of spatial noise in flame images, data filtering was performed and incorporated with the deconvolution process. The data filtering includes two steps. The filtered grey level of a specific radial profile is obtained by averaging five neighboring radial profiles. Then in the radial direction, the gray level at a specific pixel on a radial profile is replaced by the linear combination of the grey level on five neighboring pixels. The following equation shows the weighing coefficients used in the radial filtering.

$$G_i = 0.125(g_{i-2} + g_{i+2}) + 0.25(g_{i-1} + g_i + g_{i+1}), \quad (1)$$

where G_i and g_i are the gray levels at the i-th pixel after and before filtering, respectively.

In the radial direction, the data filtering was incorporated in the Abel transform according to the Filtered Abel Transform of Yuan [64]. This method first computes an integral kernel based on the desired filtering function and then convolves the kernel with radial profiles of the flame image to obtain the spatial distribution of flame properties.

Experimental uncertainties for the soot volume fraction measurements arise mostly from spatial noise in the laser images. In the flame regions, the noise is less than 10% of the average value of image gray levels. The errors from other sources, such as image digitization and round-off errors of data manipulation, etc., are orders of magnitude smaller, thus the estimated uncertainties of the soot volume fraction measurements are 10%. The images associated with the soot temperature measurements are less noisy owing to simpler optics. Assuming all individual error sources are independent, i.e., they are orthogonal in a vector space, the combined uncertainties are estimated to be ±50 K, which is typical for two-line pyrometers. This corresponds to less than 4% error in Kelvin scale. Uncertainties of the mixture fractions are derived from those of temperature measurement. If the mixture fraction is assumed to be proportional to temperature as the Zel'dovich formulation does, the uncertainties of the mixture fractions would be less than 4%. But in practical flames radiation heat loss and finite kinetics affect the correlation between the mixture fraction and flame temperature. Taking these effects into account, the uncertainties of the mixture fractions are estimated to be less than 10%. The soot volume fractions and soot temperatures, from which mixture fractions were derived, were independently measured. Thus the uncertainty of the correlation between the soot volume fraction and mixture fraction is the vectorial sum of the two uncertainties, i.e., 14.1%.

3. Analytical

The development of Spalding [56] is extended here to estimate streamline locations and residence times in the present flames. The results of this analysis help explain why soot state relationships can be expected in microgravity (but not normal gravity) gas–jet flames. Although similar results could be obtained with a computational reacting flow code, the present solution yields concise scaling laws governing streamline locations and residence times of microgravity gas–jet flames.

In the Spalding solution [56], the velocity component in the axial direction is

$$u = \frac{3}{4}\frac{I_u}{z}\left(1+\frac{\xi^2}{4}\right)^{-2}, \tag{2}$$

where

$$\xi \equiv \left(\frac{3}{8}\frac{I_u}{\nu}\right)^{0.5}\frac{r}{z} \tag{3}$$

and

$$I_u = u_0^2 d^2/(8\nu), \tag{4}$$

with u_0, d and ν being the velocity at the nozzle, the nozzle diameter and the kinematic viscosity of the fuel, respectively.

Streamline equations can be obtained by considering the volumetric flow rate bounded by the streamtube passing through the point (r,z):

$$\eta q_0 = \int_0^{r(z)} 2\pi r u\, dr, \tag{5}$$

where η is a dimensionless parameter that equals the volumetric flow rate bounded by the streamtube divided by the total volumetric flow rate issued from the burner. Note that $\eta = 1$ corresponds to the dividing streamtube, and values of η less than and greater than unity define internal and external streamlines, respectively. Streamline equations are thus obtained by solving for $r(z)$ in Eq. (5) at various z locations for a fixed value of η. By inserting the axial velocities of Eq. (2) into Eq. (5) and carrying out the integration, the following equation for streamline radius as a function of z and η is obtained:

$$\frac{r(z)}{d} = \left[\frac{3Re}{8}\frac{d}{z}\left(\frac{1}{\eta}-\frac{Re}{32}\frac{d}{z}\right)\right]^{-0.5}, \tag{6}$$

where Re is the Reynolds number at the burner exit.

In actual flames, all internal streamlines originate within the burner tube. However, the Spalding solution is not valid for small z [56]. As a result, the internal streamlines described by Eq. (6) do not originate within the burner, instead, each streamline starts as a pure radial inflow, from a far field point with infinite r and a minimum z ($z = \eta Re\, d/32$). To overcome this problem, Eq. (6) is modified here for small z by blending its behavior at large z with expected behavior at the burner exit plane. For large z, i.e., $z \gg \eta Re\, d/32$, Eq. (6) can be approximated as

$$\frac{r(z)}{d} = \left(\frac{8\eta}{3Re}\frac{z}{d}\right)^{0.5}. \tag{7}$$

Eq. (7) yields finite values of $r(z)$ for any $z \geqslant 0$, but it indicates a zero streamline radius for all the streamlines at the burner exit plane, where $z = 0$. To correct this, the ratio z/d in Eq. (7) is incremented by a small constant, $3Re/32$, thus yielding the following streamline equation:

$$\frac{r(z)}{d} = \eta^{0.5}\left(\frac{8}{3Re}\frac{z}{d}+0.25\right)^{0.5}. \tag{8}$$

This blended streamline equation yields a much better match of expected streamline behavior in the region near the nozzle and it matches the streamlines described by Eq. (6) in the limit of large z.

This streamline analysis assumes flow of an isothermal monocomponent gas. Applying Eq. (8) to gas–jet flames requires a few assumptions, as follows. First, a characteristic species and a characteristic temperature, T_{ch}, are selected. The characteristic species selected here is N_2. The T_{ch} is selected as 1334 K, which is the mean of the ambient and adiabatic flame temperatures for ethylene/air. The associated characteristic kinematic viscosity is ν_{ch}. Thermal expansion is accommodated by considering a larger burner, with diameter d_{ch}, such that the burner mass flow rate and velocity (and thus momentum) match those of ethylene at 298 K for the actual flame. The resulting characteristic diameter and Reynolds number, d_{ch}, and Re_{ch}, are

$$d_{ch} = d(T_{ch}/298\ \mathrm{K})^{0.5}, \quad Re_{ch} = Re(T_{ch}/298\ \mathrm{K})^{0.5}\nu/\nu_{ch}, \tag{9}$$

where Re is the actual Reynolds number (see Table 1), and is based on d, the actual burner diameter, and ν, the fuel viscosity at 298 K. Eq. (8) thus leads to the final equation for the dividing streamline, as follows:

$$\frac{r(z)}{d} = \left(\frac{8}{3Re_{ch}}\frac{z}{d_{ch}}+0.25\right)^{0.5}. \tag{10}$$

4. Results and discussion

Given the acceptable predictions of the extended Spalding [56] model of the shapes of non-buoyant round laminar jet diffusion flames [57], the above streamline predictions of this model were considered. Fig. 1 shows the luminous boundary for flame 03E94 in Table 1. Also shown is the predicted dividing streamline for this

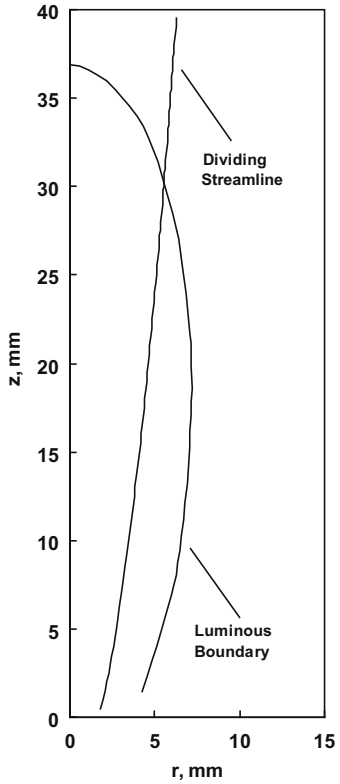

Fig. 1. Measured luminous boundary from video image and predicted dividing streamline for flame 03E94. The dividing streamline is the streamline emerging at the burner tip and was developed by extending the model of Spalding [56].

flame, from Eq. (10). Fig. 1 indicates that the dividing streamline bounds a large fraction of the soot containing region. In the corresponding normal gravity flame, the dividing streamline is expected to bound a much smaller fraction of the soot region. Velocity measurements in microgravity gas jet flames are not available, but past numerical predictions support these distinctions between dividing streamline behavior in flames in microgravity [65,66] and in normal gravity [65,67].

The unique structure of non-buoyant flames provides a large region where the mixture fraction to residence time relationship shows little variation. Given fast reactions this facilitates state relationships. Internal streamlines pass through the flame sheet once and encounter continuously decreasing mixture fractions. Fig. 2 shows a hypothesized state relationship for residence time in a non-buoyant gas jet flame. The equation and curve shown for the centerline residence time come from the integration of the velocity solution of Spalding [56]. Also shown is the estimated residence time of the dividing streamline of Fig. 1. All internal streamlines are bounded by these two curves. As Fig. 2 illustrates, all the internal streamlines have nearly identical variations of mixture fraction as a function of time after leaving the burner exit. This behavior occurs because flows near the burner axis move at the largest velocities but must travel the largest distances to reach a given mixture fraction, whereas flows near the dividing streamline move at the smallest velocities but also travel the smallest distances to reach the flame. This result is independent of the initial burner exit velocity because varying the exit velocity proportionally increases or decreases the distances traveled to reach a particular mixture fraction.

The residence time of a sample external streamline is also shown in Fig. 2. External streamlines are normalized here to zero time at their first flame crossing point. These streamlines pass twice through the flame sheet, encountering a non-monotonic variation of mixture fraction. Each external streamline has a different relationship between time and mixture fraction, which would not be expected to yield a universal state relationship.

Recalling that scalar gaseous properties in soot-containing laminar jet diffusion flames satisfy state relationships (including temperatures) as long as characteristic flame residence times are short enough so that radiant heat losses are small [4,5], this behavior implies that the reactive environment of soot particles along all paths through the flame are identical functions of time for given initial flame reactant compositions, temperatures and pressures. As a result, the question addressed by these experiments was whether, despite slow soot reaction and diffusion rates, non-buoyant laminar diffusion flames exhibit universal soot properties as a function of mixture fraction, for given initial flame reactant compositions, temperatures, and pressure, as required for the presence of soot property state relationships.

Radiation intensity images and laser extinction images, obtained at quasi-steady periods when no adjustment to the flame conditions were done by the Space Shuttle crew and, for times reported in Table 1, are shown in Fig. 3. The radiation intensity images came from the black and white video cameras that were fitted with 10 nm band pass filters at 650 and 850 nm. Only the 650 nm images are shown since the 850 nm images look very similar. Notable in the images is that all of the flames except 03E83 and 08P107 are closed tip while the 03E83 and 08P107 show no luminosity at the flame tip, suggesting local extinction. Also shown are enhanced-contrast images for the laser extinction system. The raw images show a black shadow of the soot on a light background, however the soot can be hard to discern in printed images. To improve the visibility, the background reference images were subtracted from each image and the contrast of the resultant image was enhanced with soot containing regions appearing white. Clearly evident is the soot escaping from the open tip flames (03E83 and 08P107).

Measurements of the soot temperatures and soot volume fractions of the seven flames of Table 1 are shown in Figs. 4 to 6. These figures present radial distributions at selected axial distances from the nozzle exit. Measurements are available only where soot temperatures and soot volume fractions are sufficiently high and generally are not reported near the flame centerline, where deconvolution errors lead to large uncertainties. Overall the data follow expected trends. In Fig. 4, the lower pressure 17E94

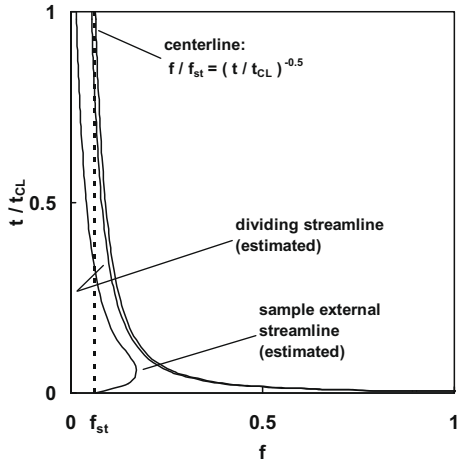

Fig. 2. Hypothesized residence time state relationship for internal streamlines. The abscissa is mixture fraction and the ordinate is residence time non-dimensionalized by the centerline residence time, t_{CL}. For external streamlines, residence time is referenced to the first crossing of the flame sheet.

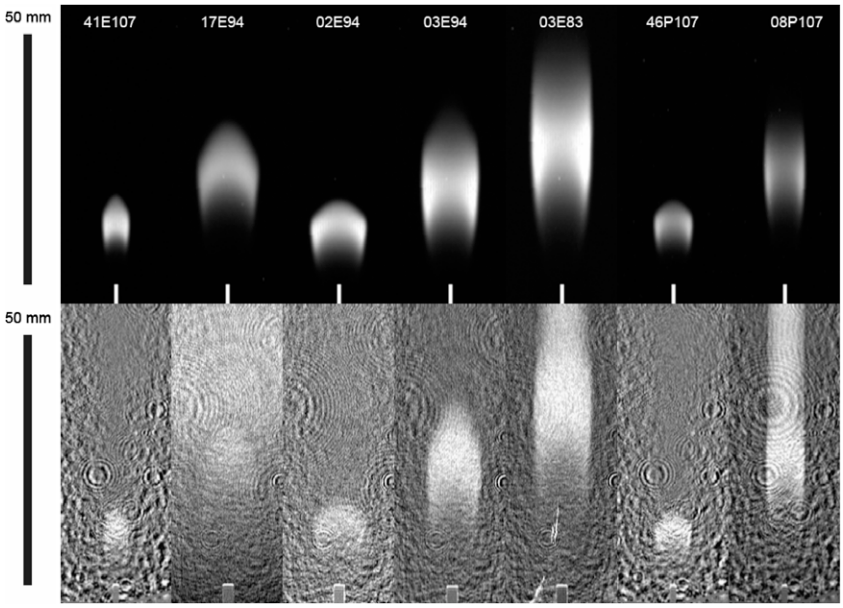

Fig. 3. Assembled soot emission images (top) with soot volume fraction images via laser extinction images (bottom) for each of the flames deconvolved in this paper. The images correspond vertically for each flame and were taken at the times indicated in Table 1. The soot emission images were taken with a 650 nm filter and the soot volume fraction images were taken using a laser line filter. The laser background (no flame present) was subtracted from each image and each image was separately contrast enhanced with soot containing regions appearing white. The ripple and interference patterns in the laser extinction images are a result of the coherent light source.

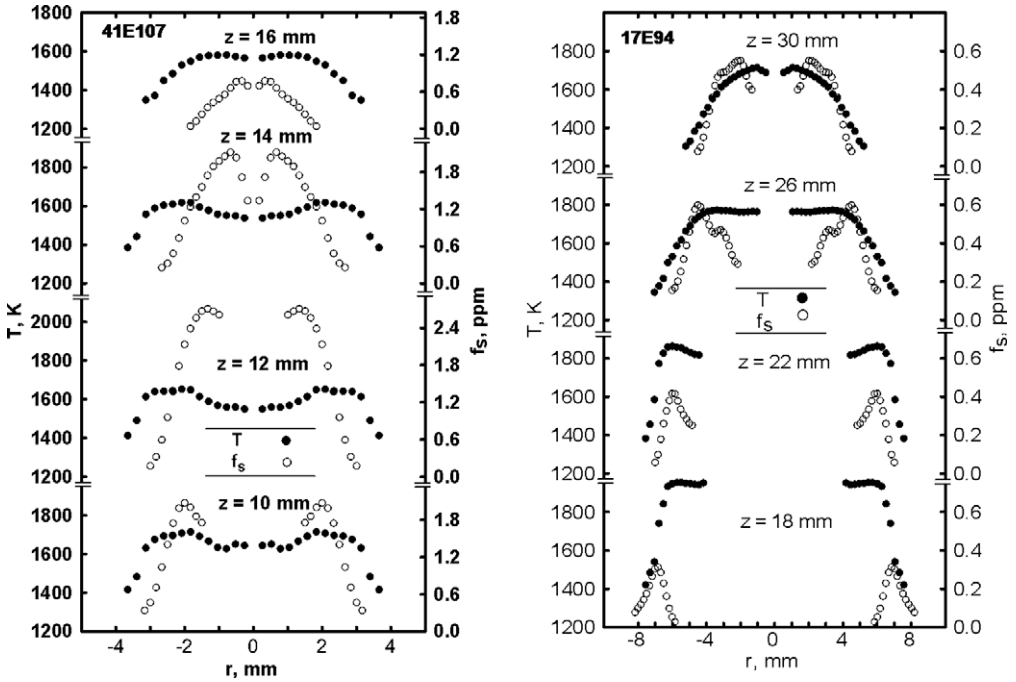

Fig. 4. Soot temperature and soot volume fraction distributions for ethylene flames at different pressures and nozzle diameters. 41E107 (d = 0.8 mm, 100 kPa, L_f = 17 mm), 17E94 (d = 1.6 mm, 35 kPa, L_f = 34.0 mm). Both sides of the flames were averaged together, however symmetric sides are shown for visibility.

(0.35 kPa) has much lower soot concentrations than the smaller 41E107 (100 kPa). In this case the pressure reduction overwhelmed the effect of the reduced velocities caused by the larger fuel jet for 17E94. Comparison of 17E94 (35 kPa – Fig. 4) with 03E94 (50 kPa – Fig. 5) shows an increase in soot concentrations and a reduction in temperature, as pressure is increased, for otherwise similar conditions (1.6 mm nozzle) and nearly equivalent mass flow rates. The increase in soot concentration is supported by the appearance of the flame tip of 03E94 (Fig. 3) which is just above the smoke point. This increased soot concentration with lower temperatures is consistent with both the increased residence time and kinetic effects of increased pressure. Fig. 5 show the progression of soot concentrations and temperatures as the fuel flow rate is increased at 0.5 kPa for the 1.6 mm nozzle, ranging from well below the smoke point (02E94), through just at the smoke point (03E94) to well above the smoke point (03E83). Notably as the soot concentrations rise by a factor of over 5 while the peak temperatures in the lower portion of the flame remain fairly

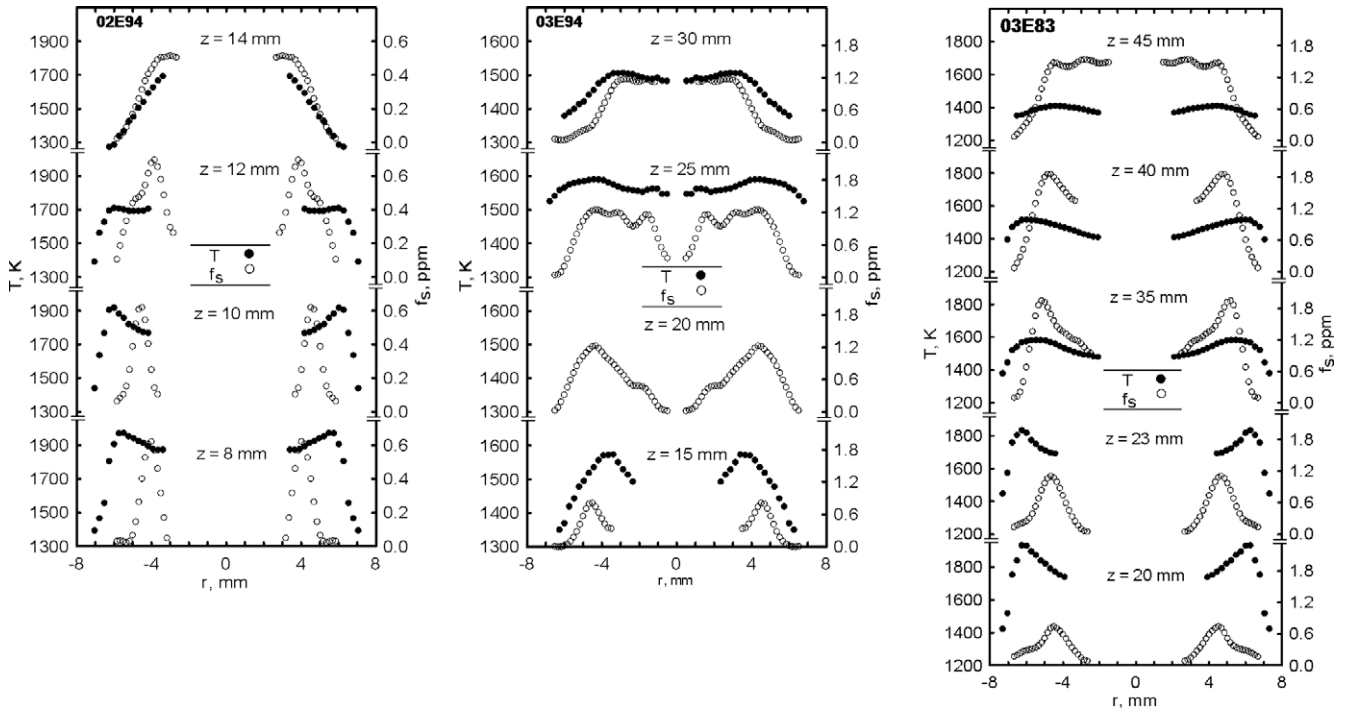

Fig. 5. Soot temperature and soot volume fraction distributions for ethylene flames with $d = 1.6$ mm at 50 kPa: 02E94 ($L_f = 17.7$ mm), 03E94 ($L_f = 36.5$ mm), and 03E83 (L = 63.0). 02E94 is below the smoke point, 03E94 is just at the smoke point, and 03E83 is well above the smoke point. Both sides of the flames were averaged together, however symmetric sides are shown for visibility.

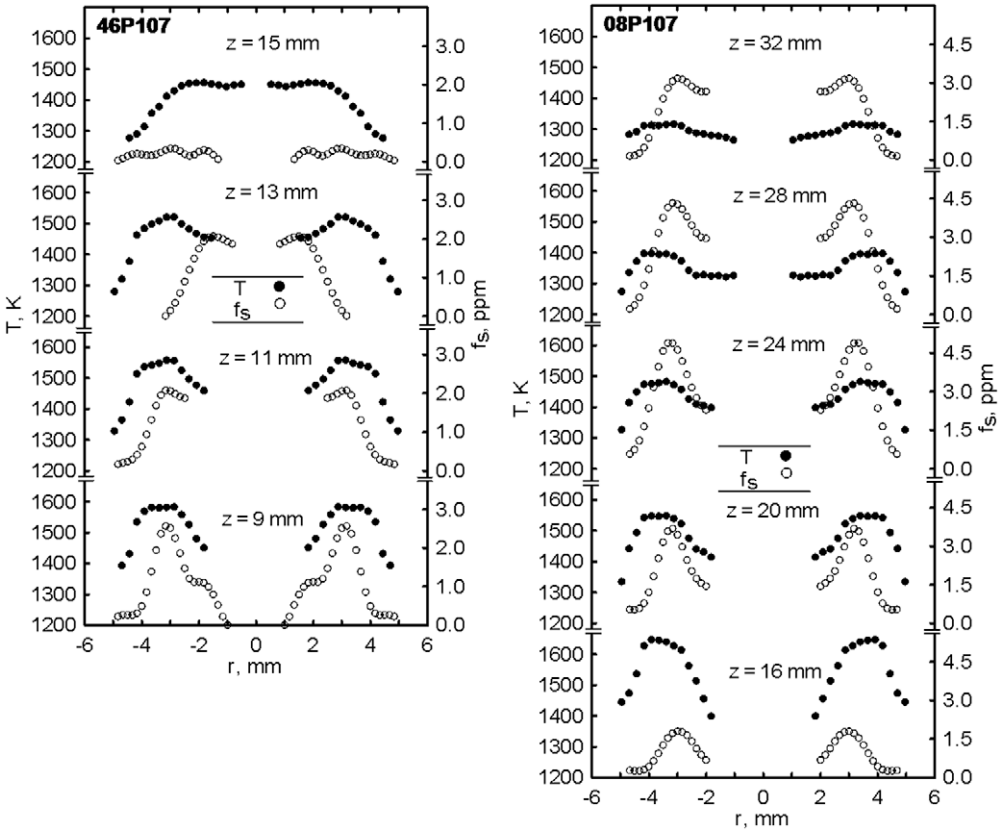

Fig. 6. Soot temperature and soot volume fraction distributions for propane flames with $d = 0.8$ mm at 99 to 100 kPa: 46P107 (99 kPa, $L_f = 15.8$ mm), and 08P107 (100 kPa, $L_f = 32.1$ mm). 46P107 is well below the smoke point and 08P107 is substantially above the smoke point (Fig. 3). Both sides of the flames were averaged together, however symmetric sides are shown for visibility.

constant, the temperature at the flame tip drops from 1700 to 1400 K. Similar behavior is seen for propane in Fig. 6 where, as the flame crosses the smoke point, the soot concentrations rise while the tip temperature drops.

Radial profiles of both soot temperature and soot volume fraction have peaks off-centerline at small axial distances. At larger distances these peaks generally converge to the centerline (e.g., flame 41E107 in Fig. 4), although soot peaks do not converge for flames that emit soot (e.g., flame 03E83 in Fig. 5). The peak temperatures of the flames typically decrease with increasing axial distance from the nozzle exit. This is attributed to radiative heat losses except at the largest axial distances, where all stations are on the oxidizer side of the flame sheet where cessation of heat release contributes with the radiative loss in cooling the gases (e.g., the z = 15 mm profile of flame 46P107 in Fig. 6).

The measurements of Figs. 4 to 6 suggest the existence of soot state relationships for some regions of these flames. The general behavior of the soot volume fraction measurements (see flame 03E83 in Fig. 5) is that peak soot volume fraction initially increases with height, then reaches a plateau, and finally decreases at axial distances beyond the stoichiometric flame tip. The plateau region is evident for all the flames in Figs. 4 to 6 and strongly suggests the existence of soot state relationships. Such state relationships are not expected at small axial distances, where external streamlines passing through the flame sheet (see discussion in connection with Figs. 1 and 2), heat losses to the burner, air leakage through the flame base, and limited residence time combine to limit soot volume fraction. The majority of streamlines originating from the burner pass through the plateau region and exhibit nearly the same maximum soot concentration, which follows if the reaction environment is the same function of time for all interior streamlines.

This behavior is demonstrated in Fig. 7, which shows the maximum soot volume fraction and the maximum temperature at each axial location in Figs. 4 to 6 for the present flames. These maximum values are normalized by the highest value observed in each flame and are plotted as functions of normalized axial location. The slow decrease of normalized peak temperature with increasing axial distance, evident in Fig. 7, is attributed to radiative heat losses. The outlying profile was for the strongly soot emitting 03E83 where radiative cooling dominated heat release. The normalized soot volume fraction increases quickly near the nozzle, reaches a plateau and then decreases again near the luminous flame tip. In the central portion of the flame (away from the burner influenced region and away from the soot oxidation region in the flame tip) the soot volume fraction and soot temperature levels are uniform. Given the aforementioned uniformity of residence time and mixture fraction for internal streamlines, these findings are expected and they support the existence of soot state relationships in these flames.

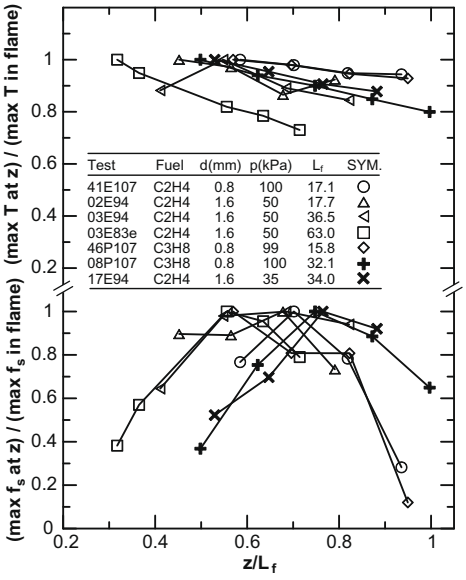

Fig. 7. Peak soot volume fraction and temperature normalized by the corresponding maximum value observed within each flame as a function of streamwise distance normalized by the luminous flame length.

The present measurements allow soot state relationships – correlations between mixture fraction and soot volume fraction – to be considered in regions where both soot temperature and soot volume fraction were measured. To avoid complications associated with partial premixing, only attached flames are considered here. Mixture fractions were not measured directly but instead were estimated from measured temperatures as follows. Temperatures were linearly interpolated at the locations of measured soot volume fractions and temperatures. Locations were considered to be on the fuel/oxidizer side of the flame if they were inside/outside the contour of peak temperature. A peak temperature was identified at each height in each flame and was assumed to correspond to stoichiometric conditions. For profiles with no peak temperature (e.g., 02E94, z = 14 mm) the peak (stoichiometric) temperature was assumed to be that of the next lower temperature profile with a peak temperature. Mixture fractions were then estimated, assuming linear relationships between temperature and mixture fraction at each height and on both sides of the flame, ranging from stoichiometric conditions at the peak temperature to either the ambient conditions for the lean side or the nozzle conditions for the rich side. Such linearity is predicted by Burke and Schumann [12] and by activation-energy asymptotics [3].

Soot state relationships were examined for each fuel/pressure combination among the attached flames of Table 1. The results are shown in Fig. 8 for ethylene and Fig. 9 for propane. Log scales were used for the y axes of Figs. 8 and 9 to resolve the data on the lean side of the flames, where soot volume fraction varies by up to two orders of magnitude. Data from small heights were excluded here owing to effects of external streamlines, partial premixing and burner tube heat loss.

Figs. 8 and 9 reveal peak soot volume fractions at or near the flame sheet, a steep decline on the oxidizer side, and a relatively constant region on the fuel side. These relationships do not extend to very lean regions, where soot volume fractions were too low to measure, or to very rich regions, where temperatures were too low to measure. These relationships can be used to predict soot concentration for a given mixture fraction in a suitable flame, although this may present difficulties in lean regions owing to steepness in the correlations.

The correlation of the data in Figs. 8 and 9 is better than past soot state relationships in buoyant diffusion flames [5,44,45]. The data fit of Gore and Faeth [45] is shown for laminar ethylene flames at 100 kPa. It agrees with the peak soot volume fraction and the steep decline toward the oxidizer, but is shifted toward the rich side.

Soot state relationships are not widely accepted for turbulent non-premixed flames. This is because soot production can be highly sensitive to the scalar dissipation rate. (Compositions of lighter species are less sensitive to the scalar dissipation rate and thus are more likely to follow state relationships in turbulent flames.) Many turbulent flames have widely varying scalar dissipation rates, possibly varying between the limits of kinetic and radiative extinction. The present flames contain a moderate range of scalar dissipation rates, and yield reasonable soot state relationships. This suggests that turbulent flames for which most of the reaction occurs in regions with limited ranges of scalar dissipation rates should obey the soot state relationships found here. Implementation of soot state relationships would have the potential of substantial computational cost savings for combustion modeling.

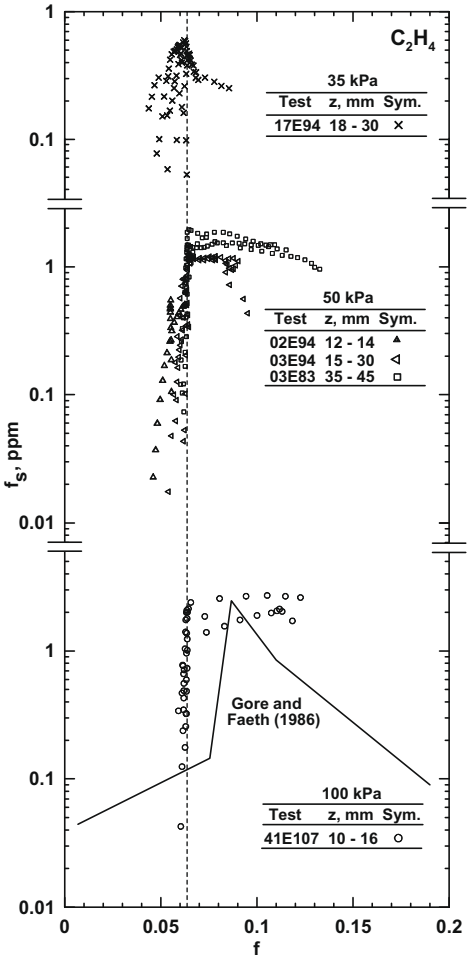

Fig. 8. Soot state relationships for the present ethylene flames at 35, 50 and 100 kPa. The vertical dashed line corresponds to the flame sheet (f_{st} = 0.0636).

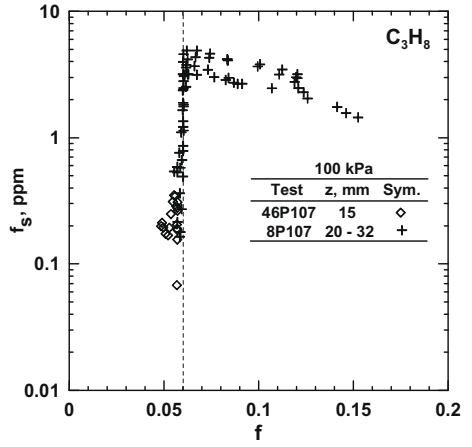

Fig. 9. Soot state relationship for the present propane flames at 100 kPa. The vertical dashed line corresponds to the flame sheet (f_{st} = 0.0602).

5. Conclusions

Experimental observations of non-buoyant round laminar jet diffusion flames were made for the following test conditions: ethylene and propane burning in still air; ambient temperature of 298 K; ambient pressures of 35–100 kPa; jet exit diameters of 0.8–1.6 mm; jet exit Reynolds numbers of 57–229; luminous flame length to burner diameter ratios of 11–125; and luminous flame lengths of 16–63 mm. These observations have yielded the following major conclusions:

1. For the present non-buoyant flames the majority of the flame volume is inside the dividing streamlines. In these regions, the analysis of streamlines based on an extension of Spalding's model suggests the existence of a state relationship for time, and consequently suggests a state relationship also exists for soot.
2. Maximum soot volume fractions and flame temperatures were similar for all paths from the burner exit through the flame sheet for closed-tip flames having small radiative heat losses. This is a necessary condition for the existence of soot property state relationships for steady non-buoyant laminar diffusion flames, and thus in practical turbulent diffusion flames through the application of the laminar flamelet concept.
3. In regions not affected by heat loss to the burner and excluding the flame tip, peak soot volume fraction and soot temperature did not vary strongly with axial distance. This result further supports the assertion that state-relationship behavior is possible for soot in non-buoyant flames.
4. Reasonable soot state relationships were found for ethylene flames at 35, 50 and 100 kPa and for propane flames at 100 kPa. The present relationships had peak soot volume fractions at or near the flame sheet, a steep decline on the oxidizer side, and a relatively constant region on the fuel side. The correlations have less scatter than past soot state relationships for buoyant flames.

Most practical turbulent diffusion flames are non-buoyant on a local basis, although flame motion in large scale is affected by buoyancy; therefore, universal soot property state relationships should be observed for a relatively large class of practical soot-containing turbulent diffusion flames.

Acknowledgments

This research was sponsored by NASA Grant NAG3-2404 under the technical management of the NASA Glenn Research Center. The authors acknowledge the contributions of Ann Over and her associates at the NASA Glenn Research Center for development of the test apparatus and the crews of Space Shuttle Columbia flights STS-83 94 and 107, who performed the experiments in orbit.

References

[1] A.C. Revkin, New York Times, April 21, 2001.
[2] D.O. Lignell, J.H. Chen, P.J. Smith, Y. Lu, C.K. Law, Combust. Flame 151 (2007) 2–28.
[3] F.A. Williams, Prog. Energy Combust. Sci. 26 (2000) 657–682.
[4] G.M. Faeth, G.S. Samuelsen, Prog. Energy Combust. Sci. 12 (1986) 305–372.
[5] J.P. Gore, G.M. Faeth, J. Heat Transfer 110 (1988) 173–181.
[6] F. Mauss, K. Netzell, H. Lehtiniemi, Combust. Sci. Technol. 178 (2006) 1871–1885.
[7] F. Liu, H. Guo, G.J. Smallwood, Combust. Flame 144 (2006) 605–618.
[8] H. Richter, J.B. Howard, Prog. Energy Combust. Sci. 26 (2000) 562–611.
[9] I.M. Kennedy, Prog. Energy Combust. Sci. 23 (1997) 95–132.
[10] C.W. Lautenberger, J.L. de Ris, N.A. Dembsey, J.R. Barnett, H.R. Baum, Fire Safety J. 40 (2005) 141–176.
[11] Z.A. Mansurov, Combust. Expl. Shock Waves 41 (2005) 727–744.
[12] S.P. Burke, T.E.W. Schumann, Ind. Eng. Chem. 20 (1928) 998–1004.
[13] J.B. Haggard, T.H. Cochran, Combust. Sci. Technol. 5 (1972) 291–298.
[14] M.Y. Bahadori, R.B. Edelman, D.P. Stocker, S.L. Olson, AIAA J. 28 (1990) 236–244.
[15] G. Legros, P. Joulain, J. Vantelon, A. Fuentes, D. Bertheau, J.L. Torero, Combust. Sci. Technol. 178 (2006) 813–835.
[16] A. Fuentes, S. Rouvreau, P. Joulain, J.-P. Vantelon, G. Legros, J.L. Torero, A.C. Fernandez-Pello, Combust. Sci. Technol. 179 (2007) 3–19.

[17] A. Yozgatligil, S.-H. Park, M.Y. Choi, Combust. Sci. Technol. 176 (2004) 1985–1999.
[18] P.B. Sunderland, D.L. Urban, D.P. Stocker, B.-H. Chao, R.L. Axelbaum, Combust. Sci. Technol. 176 (2004) 2143–2164.
[19] R.W. Bilger, Prog. Energy Combust. Sci. 1 (1976) 87–109.
[20] F.C. Lockwood, A.S. Naguib, Combust. Flame 24 (1975) 109–124.
[21] R.W. Bilger, S.B. Pope, K.N.C. Bray, J.F. Driscoll, Proc. Combust. Inst. 30 (2005) 21–42.
[22] R.W. Bilger, Prog. Energy Combust. Sci. 26 (2000) 367–380.
[23] F. Maus, D. Keller, N. Peters, Proc. Combust. Inst. 23 (1990) 693–698.
[24] H. Pitsch, Combust. Flame 123 (2000) 358–374.
[25] H.-W. Ge, E. Gutheil, Combust. Flame 153 (2008) 173–185.
[26] K. Claramunt, R. Cònsul, D. Carbonell, C.D. Pérez-Segarra, Combust. Flame 145 (2006) 845–862.
[27] L. Vervisch, R. Hauguel, P. Domingo, M. Rulland, J. Turbulence 5 (2004) 2–36.
[28] A. Tewarson, in: SFPE Handbook of Fire Protection Engineering, National Fire Protection Association, Quincy, MA, 1988, pp. 1-179 to 1-199.
[29] Ü.Ö. Köylü, Y. Sivathanu, G.M. Faeth, Proc. Third International Symposium on Fire Safety Science, Elsevier, London, 1991. pp. 625–634.
[30] Ü.Ö. Köylü, G.M. Faeth, Combust. Flame 87 (1991) 61–76.
[31] J.P. Gore, S.-M. Jeng, G.M. Faeth, J. Heat Transfer 109 (1987) 165–171.
[32] M.E. Kounalakis, J.P. Gore, G.M. Faeth, Proc. Combust. Inst. 22 (1988) 1281–1290.
[33] J.P. Gore, S.-M. Jeng, G.M. Faeth, AIAA J. 25 (1987) 339–345.
[34] M.E. Kounalakis, J.P. Gore, G.M. Faeth, J. Heat Transfer 111 (1989) 1021–1030.
[35] M.E. Kounalakis, Y.R. Sivathanu, G.M. Faeth, J. Heat Transfer 113 (1991) 437–445.
[36] S.-M. Jeng, M.-C. Lai, G.M. Faeth, Combust. Sci. Technol. 40 (1984) 41–53.
[37] S.-M. Jeng, G.M. Faeth, J. Heat Transfer 106 (1984) 886–888.
[38] J.P. Gore, G.M. Faeth, D. Evans, D.B. Pfenning, Fire Mater. 10 (1986) 161–169.
[39] K. Claramunt, R. Cònsul, D. Carbonell, C.D. Pérez-Segarra, Combust. Flame 145 (2006) 845–862.
[40] M.J. Zimberg, S.H. Frankel, J.P. Gore, Y.R. Sivathanu, Combust. Flame 113 (1998) 454–469.
[41] H. Pitsch, E. Riesmeier, N. Peters, Combust. Sci. Technol. 138 (2000) 389–406.
[42] I.M. Aksit, J.B. Moss, Combust. Flame 145 (2006) 231–244.
[43] C.S. Yoo, H.G. Im, Proc. Combust. Inst. 31 (2007) 701–708.
[44] Y.R. Sivathanu, J.P. Gore, Combust. Flame 97 (1994) 161–172.
[45] J.P. Gore, G.M. Faeth, Proc. Combust. Inst. 21 (1986) 1521–1531.
[46] Y.R. Sivathanu, G.M. Faeth, Combust. Flame 81 (1990) 150–165.
[47] J.H. Kent, D. Honnery, Combust. Sci. Technol. 54 (1987) 383–397.
[48] A. D'Anna, M. Commodo, S. Violi, C. Allouis, J. Kent, Proc. Combust. Inst. 31 (2007) 621–629.
[49] D.L. Urban, Z.-G. Yuan, P.B. Sunderland, G.T. Linteris, J.E. Voss, K.-C. Lin, Z. Dai, K. Sun, G.M. Faeth, AIAA J. 36 (1998) 1346–1360.
[50] G.M. Faeth, Proc. AIAA/IKI Microgravity Science Symposium-Moscow, AIAA, Washington, 1991. pp. 281–293.
[51] C.K. Law, G.M. Faeth, Prog. Energy Combust. Sci. 20 (1994) 65–113.
[52] G.M. Faeth, in: H.D. Ross (Ed.), Microgravity Combustion Science, Academic Press, New York, 2001, pp. 83–182.
[53] P.B. Sunderland, S. Mortazavi, G.M. Faeth, D.L. Urban, Combust. Flame 96 (1994) 97–103.
[54] P.B. Sunderland, Ü.Ö. Köylü, G.M. Faeth, Combust. Flame 100 (1995) 310–322.
[55] P.B. Sunderland, G.M. Faeth, Combust. Flame 105 (1996) 132–146.
[56] D.B. Spalding, Combustion and Mass Transfer, Pergamon Press, New York, 1979. pp. 185–195.
[57] C. Aalburg, F.J. Diez, G.M. Faeth, P.B. Sunderland, D.L. Urban, Z.-G. Yuan, Combust. Flame 142 (2005) 1–16.
[58] P.B. Sunderland, B.J. Mendelson, Z.-G. Yuan, D.L. Urban, Combust. Flame 116 (1999) 376–386.
[59] K.-C. Lin, G.M. Faeth, P.B. Sunderland, D.L. Urban, Z.-G. Yuan, Combust. Flame 116 (1998) 415–431.
[60] P.B. Sunderland, S. Mortazavi, G.M. Faeth, D.L. Urban, Combust. Flame 96 (1994) 97–103.
[61] D.L. Urban, Z.-G. Yuan, P.B. Sunderland, K.-C. Lin, Z. Dai, G.M. Faeth, Proc. Combust. Inst. 28 (2000) 1965–1972.
[62] P.S. Greenberg, J.C. Ku, Appl. Opt. 36 (1997) 5514–5522.
[63] W.H. Dalzell, A.F. Sarofim, J. Heat Transfer 91 (1969) 100–104.
[64] Z.-G. Yuan, NASA/CR-2003-212121, March 2003.
[65] C.R. Kaplan, E.S. Oran, K. Kailasanath, H.D. Ross, Proc. Combust. Inst. 26 (1996) 1301–1309.
[66] A. Lock, A.M. Briones, S.K. Aggarwal, I.K. Puri, U. Hegde, Combust. Flame 149 (2007) 340–352.
[67] F. Takahashi, V. Katta, Proc. Combust. Inst. 29 (2002) 2509–2518.